

## A superfluid boundary layer

G. W. Stagg,\* N. G. Parker, and C. F. Barenghi

*Joint Quantum Centre (JQC) Durham-Newcastle, School of Mathematics and Statistics,  
Newcastle University, Newcastle upon Tyne, NE1 7RU, UK*

(Dated: September 24, 2018)

We model the superfluid flow of liquid helium over the rough surface of a wire (used to experimentally generate turbulence) profiled by atomic force microscopy. Numerical simulations of the Gross-Pitaevskii equation reveal that the sharpest features in the surface induce vortex nucleation both intrinsically (due to the raised local fluid velocity) and extrinsically (providing pinning sites to vortex lines aligned with the flow). Vortex interactions and reconnections contribute to form a dense turbulent layer of vortices with a non-classical average velocity profile which continually sheds small vortex rings into the bulk. We characterise this layer for various imposed flows. As boundary layers conventionally arise from viscous forces, this result opens up new insight into the nature of superflows.

PACS numbers: 67.30.H-, 67.30.he, 47.37.+q, 03.75.Lm

At sufficiently low temperatures, liquid helium has two striking properties. Firstly, it flows without viscosity. Secondly, its vorticity is constrained to thin mini-tornadoes, characterised by fixed circulation  $\kappa$  (the ratio of Planck's constant to the mass of the relevant boson - one atom in  $^4\text{He}$  and one Cooper pair in  $^3\text{He-B}$ ) and microscopic core radius  $\xi$  (0.1 nm in  $^4\text{He}$  and 10 nm in  $^3\text{He-B}$ ). In contrast, the eddies in everyday viscous fluids can have arbitrary shape, size and circulation.

Of ongoing experimental and theoretical study is the nature of turbulence in superfluids [1–4], a state consisting of an irregular tangle of quantised vortex lines. Despite fundamental differences between superfluids and classical fluids, the observations of Kolmogorov energy spectra (famed from classical isotropic turbulence) in superfluid turbulence [1] are suggestive of a deep connection between them. Superfluid turbulence is nowadays most commonly formed by moving obstacles, including grids [5], wires [6–9], forks [10, 11], propellers [12, 13], spheres [14] and other objects [15]. Despite progress in visualizing the flow of superfluid helium in the bulk [16, 17], including individual vortex reconnections [18], the study of flow profiles [19, 20] is still in its infancy and there is no direct experimental evidence about what happens at boundaries. Here, vortices are believed to be generated by two mechanisms. Firstly, vortices can nucleate at the boundary of the vessel or object [21]. When the relative flow speed is sufficiently low, the flow is laminar (potential) and dissipationless. Near curved boundaries, however, intrinsic vortex nucleation occurs if the local flow velocity exceeds a critical value. Secondly, the vortices can be procreated (extrinsically generated) by the ‘vortex-mill’ mechanism [22] from so-called ‘remanent vortices’ which are present in the system since cooling the helium through the superfluid transition. Remanent vortices can be avoided using judicious, slow experimental protocols [27].

The nano-scale vortex core in superfluid helium is com-

parable in size to the typical roughness of the boundaries of the vessel or stirring object. Unfortunately the lack of direct experimental information about vortex nucleation at the boundaries and the subsequent vortex-boundary interactions, limit the interpretation of experiments. Theoretical progress is challenging and to date has focussed on smooth and idealised surfaces. In principle, the superfluid boundary conditions are straightforward: the superfluid velocity component which is perpendicular to the boundary must vanish at the boundary, whereas the tangential component (in the absence of viscous stresses) can slip. For the latter reason, in superfluids we do not expect boundary layers typical of viscous flows. Implementing these superfluid boundary conditions, it was found [23, 24] that one or more vortices sliding along a smooth surface can become deflected or trapped by small hemispherical bumps. Such bumps can also serve as nucleation sites for vortices; the local superfluid velocity is raised at the pole of the bump and more readily breaks the critical velocity for vortex nucleation [25]. Indeed, our recent simulations [26] have shown that, if the bump is elliptically shaped and elongated perpendicular to the imposed flow, the superfluid velocity  $v$  at the pole is enhanced, reducing the critical Mach number for vortex nucleation from  $v/c \sim 1$  to smaller values  $v/c \sim \epsilon^{-1} \ll 1$  (where  $\epsilon \gg 1$  is the ellipticity of the bump), and increasing the intrinsic vortex nucleation rate (for a given super-critical imposed flow). We expect therefore that microscopically-small surface roughness may promote the nucleation of vortices at a surface. For pre-existing vortex lines in the vicinity of the surface, there is also indirect experimental evidence of a ‘vortex mill’ mechanism which continuously feeds vorticity into the flow by stretching any pre-existing vortex lines. This mechanism only works if the spooling vortex, held by pinning sites at the surface, is aligned in the streamwise direction [22]. In summary, boundary roughness potentially affects both intrinsic and extrinsic

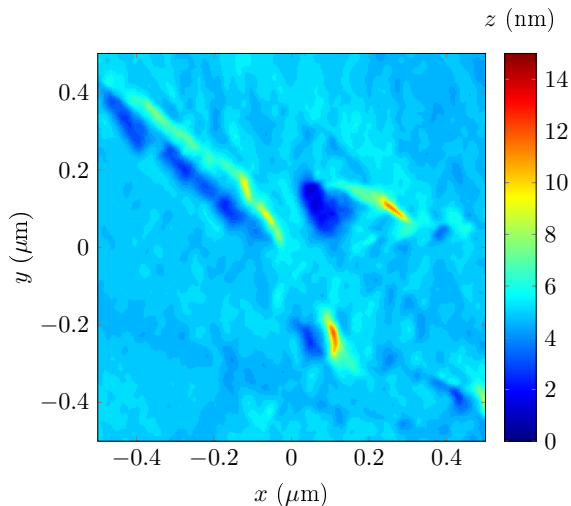


FIG. 1. AFM image of a section of the NbTi wire rough surface, smoothed by a Gaussian blur (standard deviation 6 nm) so as to remove discontinuities in the surface profile.

mechanism to create new vortices.

To shed light on the problem, we work with the 3D profile of a rough surface [Fig. 1]. This corresponds to a  $(1\mu\text{m})^2$  region of the surface of a thin NbTi wire used to generate quantum turbulence at Lancaster University, as profiled via atomic force microscopy (AFM) [28]. The surface is rough, with a height up to around 10 nm, and features sharp grooves and steep ridges, likely to have arisen during the etching phase of the wire preparation. We assume that such a ‘mountain’ landscape is typical of the wires and similar objects used in experiments.

We model the flow of superfluid helium over this surface through the time-dependent Gross-Pitaevskii equation (GPE) for a weakly-interacting Bose superfluid [29]. The GPE describes a fluid, of density  $n(\mathbf{r}, t)$  and velocity  $\mathbf{v}(\mathbf{r}, t)$ , which follows a classical continuity equation and a modified Euler equation (the modification being the presence of a quantum pressure term, arising from zero-point motion of the particles and responsible for vortex nucleation and reconnections). While the GPE provides only a qualitative model of the strongly-interacting superfluid helium (for example, the GPE’s excitation spectrum lacks helium’s roton minimum), it nevertheless contains the key microscopic physical ingredients of our problem: finite-size vortex core, vortex interactions and vortex reconnections. The more traditional vortex filament model [30], used to model the motion of vortex lines in the presence of smooth spherical [31, 32], hemispherical [23, 24] and cylindrical boundaries [33, 34], is less appropriate for a number of reasons: it assumes that the vortex core is infinitesimal compared to any other length scale (which is not the case if vortex core and wall roughness are comparable); it does not contain vortex nucleation and kinetic energy losses due to sound emission; and it is difficult to generalise from smooth, geometrically simple (cylindrical

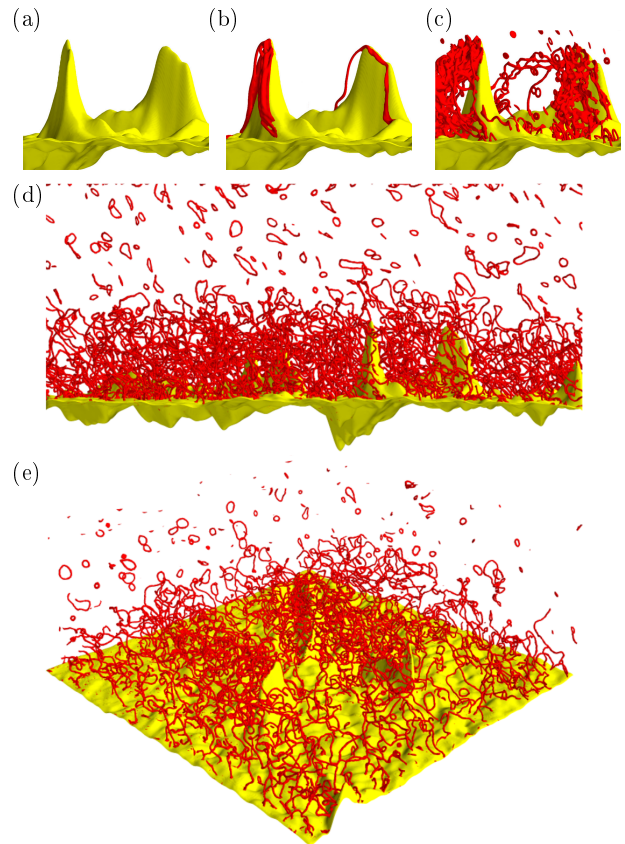


FIG. 2. Vortex nucleation and formation of the turbulent boundary layer for imposed flow  $v = 0.6c$ . (a-c) Isosurface density plots ( $0.25n_0$ ), showing the surface (yellow) and vortices (red) in the vicinity of the two tallest mountains (view taken along  $y$  for  $15\xi \leq x \leq 125\xi$ ) at times  $t = 20, 30, 100\tau$ . In (c) note three vortex lines which are aligned along the imposed flow and develop unstable Kelvin waves which will reconnect and create new vortex loops. (d-e) Isosurfaces of the entire surface in the saturated turbulent regime at late times ( $t = 1220\tau$ ). Note the turbulent layer up to approximately the height of the tallest mountains and the region of small vortex rings above it.

or spherical) boundaries to rough boundaries.

The bulk fluid has uniform average density  $n_0$ , with the surface imposed as an impenetrable region. The characteristic scales of length and speed are healing length  $\xi$  (the vortex core size) and speed of sound  $c$ , respectively. A characteristic time scale follows as  $\tau = \xi/c$ . We simulate the superfluid flowing at an imposed speed  $v$  over the entire AFM surface, in a 3D domain, periodic in  $x$  and  $y$ . The surface area  $(1\mu\text{m})^2$  is mapped onto the largest practical healing length area of  $(400\xi)^2$  [29].

In the vicinity of the surface the local fluid speed is enhanced by the surface’s roughness, with the maximum values occurring near the tallest mountains. Up to a critical speed,  $v_c$ , the flow remains vortex-free. For increased imposed flow velocity,  $v_c$  is first exceeded at the highest mountain, leading to vortex nucleation [Fig. 2 (a-c)], and

then at other high mountains on the surface. The critical velocity for vortex nucleation across this surface occurs for an imposed flow  $v_c \approx 0.2c$ ; this is considerably smaller than, say a hemispherical bump for which  $v_c \approx 0.5c$  [25], indicating the significant role of the surface roughness in enhancing the breakdown of laminar flow.

We focus on the imposed flow speeds  $v = 0.3c, 0.6c$  and  $0.9c$ , each well exceeding  $v_c$ . Nucleated vortices either peel off the boundary or, more frequently, slide down the slopes of the mountains in the form of partially attached vortex loops (carried by the imposed flow). Nucleated vortex loops are of the same circulation and form clusters (manifesting as partially attached vortex bundles) on the leeward side of the mountains, see Fig. 2(b). The velocity field of vortex bundles and the nucleation of small vortex loops throughout the surface cause vortex stretching and reconnections, distorting the bundles of vortices and small rings into a complex tangle downstream of the mountains. The tangle is continuously fed by further vortices which are generated. The formation of the tangle is shown in Fig. 2(c), and the fully developed turbulent layer near the surface is seen in Fig. 2(d-e).

As the number of vortices increases, the turbulent region remains strongly localised near the surface, up to approximately the height of the tallest mountain, forming a distinct layer [Fig. 2(d)]. Vortex reconnections cause a continuous ejection of vortex rings which spread into the bulk [Fig. 2(d, e)]. These small rings, predicted by [35, 36], play an important role in turbulent cascades [37].

The turbulent layer and ejected vortex rings are not isotropic: on average, vortex lines tend to be flattened, parallel to the surface; the ejected rings also tend to lie more in the  $xy$  plane (and travel vertically away from the layer).

We monitor the vortex line length below the tallest mountain ( $z \approx 100\xi$ ),  $L_0$ , and above it,  $L_1$  [Fig. 3 (inset)]. For  $v = 0.6c$ ,  $L_0$  increases with time and saturates. Meanwhile,  $L_1$  rises slowly, as small rings are continually shed by the turbulent layer into the bulk. Repeating for slower ( $v = 0.3c$ ) and faster ( $v = 0.9c$ ) imposed flows reveals the same qualitative behaviour, but where the layer forms at a slower and faster rate, respectively. The resulting vortex line length distribution is shown in Fig. 3. The vortices are predominately located near the surface of the wire, with a faster imposed flow leading to denser turbulent layers.

At early times, vortex lines which become aligned along the flow direction may twist and generate further vortices. Surface roughness favours this effect by providing pinning sites for streamwise-aligned vortices which develop Kelvin waves and reconnect, spooling new vorticity. An example of this vortex-mill mechanism [22] can be seen in Fig. 2 (c). This confirms that the vortex tangle which develops can be interpreted as generated either intrinsically, or extrinsically by the vortex-mill mechanism:

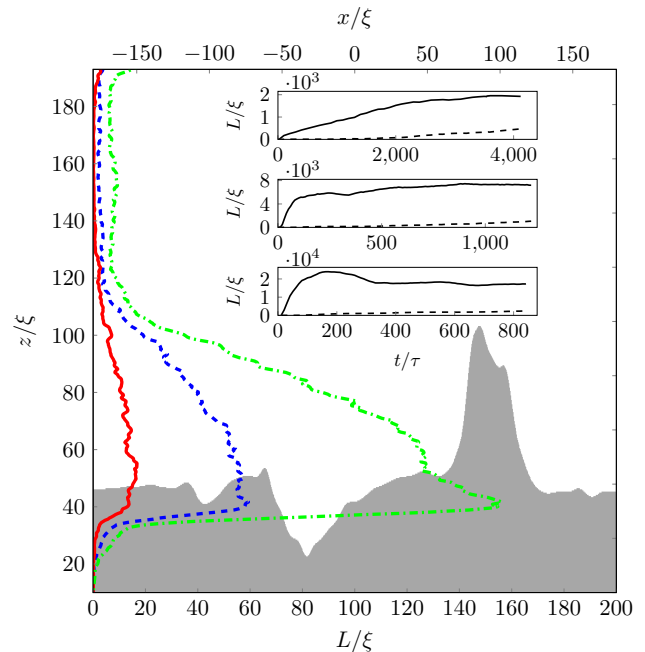


FIG. 3. Average vortex line length,  $L$  (bottom scale), as a function of height,  $z$  (left scale), for  $v = 0.3c$  (solid red line),  $v = 0.6c$  (dashed blue line), and  $v = 0.9c$  (dot-dashed green line) in the saturated regime. A 2D slice ( $y = 0.1 \mu\text{m}$ ) of the 3D surface along  $x$  (top scale) is shown in grey to visualize the height of the highest mountains. Inset: Vortex line length below ( $L_0$ , solid line) and above ( $L_1$ , dashed line) the height of  $z = 100\xi$  (approximately the height of the highest mountain) for imposed flow speeds  $v = 0.3c$  (top),  $0.6c$  (middle) and  $0.9c$  (bottom).

in both cases vortices nucleate at the tallest mountains before filling the layer below.

At later times (when the turbulent layer of vortices has saturated) and/or for higher imposed flow velocities, the critical velocity is exceeded across greater areas of the surface. However, the highest mountains continue to dominate vortex generation; here the fluid velocity is always the highest and vortex shedding occurs at the fastest rate. To maintain equilibrium, vortex line-length is continuously ejected from the top of the turbulent layer by vortex twisting and reconnections which create small vortex rings that detach and travel upwards in the positive  $z$  direction. An example is seen in Fig. 4, and highlights the role of reconnections (hence of the quantum pressure) in creating new vortices.

To characterise the turbulent layer in a quantitative way, we determine the average turbulent velocity  $\langle v \rangle$  [38] as a function of height  $z$  for the three imposed flow speeds [Fig. 5]. In all cases the turbulent layer consists of three regions. In the top region  $100\xi \lesssim z \lesssim 200\xi$ ,  $\langle v \rangle$  is equal to the velocity of the applied flow, showing that, above the height of the tallest mountain, the flow is unaffected by the rough surface underneath. In the middle region  $40 \lesssim z \lesssim 100\xi$ , the presence of vortices near the surface

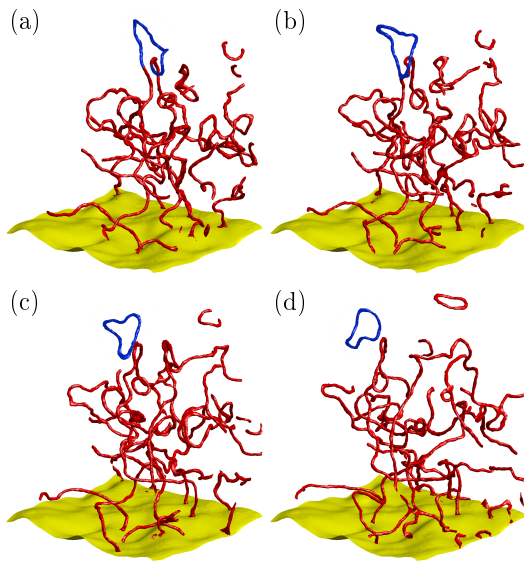


FIG. 4. Extrinsic nucleation of a vortex ring (highlighted in blue) from the boundary layer, which escapes into the bulk. As for Fig. 2 but zoomed up on a  $(76\xi)^2$  region of the surface at times  $t = 730, 640, 750$  and  $770 \tau$ .

creates a velocity field that counteracts the imposed flow: the closer to the surface one is, the slower  $\langle v \rangle$  is. In the bottom region  $0 \lesssim z \lesssim 40\xi$ , most of the computational volume is below the average surface, and only the fluid in the valleys contributes to  $\langle v \rangle$ , which rapidly drops to near zero.

The difference between the energy which is fed into the turbulent layer by the incoming (uniform) flow profile and the energy removed by the (approximately linear) profile is the energy dissipated into sound waves [39, 40]. In classical turbulence, the energy dissipation can be related to the kinematic viscosity  $\nu$  of the fluid. In our problem, we estimate [29] that the emergent  $\nu$  is  $\nu/\kappa \approx 2.4, 1.5$  and  $1.1$  at the three imposed flow speeds, larger than  $\nu/\kappa \approx 0.1$  reported in  $\text{He}^4$  experiments[41]. However, in our problem the vortex lines are much closer to each other, relative to the vortex core size: the ratio of the average vortex distance  $\delta \approx \mathcal{L}^{-1/2}$  and vortex core radius  $a_0$  at the three imposed speeds is  $\delta/a_0 \approx 13.8, 7.4$  and  $5.1$ , whereas  $\delta/a_0 \approx 2 \times 10^6$  is typical of  $\text{He}^4$  experiments [29]. Stronger accelerations and more frequent reconnections justify the larger dissipation in our problem.

The analogy with classical fluids was recently pursued by the introduction of the superfluid Reynolds number [42, 43]  $Re_s = (v - v_c)D/\kappa$  (where  $D$  is the length scale of the problem), Quasi-classical flows (such as Karman vortex street configurations for the flow past an obstacle [26, 42, 44, 45]) appear only if  $Re_s$  is sufficiently large. 2D simulations [42] suggest that turbulence onsets for  $Re_s > Re_c = 0.7$  (the Karman vortex streets becoming

irregular). In our case  $D = 60\xi$  and  $\kappa = 2\pi c\xi$ ; for the three applied flow speeds we find  $Re_s \approx 1.0, 3.8, 6.7$ , all larger than the cited  $Re_c$ , which is to be expected since we have developed turbulence.

In classical fluid dynamics boundary layers arise from viscous forces which are absent in low temperature superfluid helium. A classical fluid boundary layer is either laminar or turbulent, and it is natural to ask whether there is any transition from laminar to turbulent boundary layer for our problem. In classical laminar flow, sheets of fluid slide past each other, smoothly exchanging momentum and energy only via molecular collisions at the microscopic scale; in the turbulent case, eddies induce mixing across sheets which are macroscopically separated from each other. The superfluid analog of laminar flow is potential (vortex-free) flow. Our simulations show either vortex-free flow or turbulent flows past the rough surface, so they describe a transition from laminar flow to developed turbulence. The bottom region of fluid ( $0 \lesssim z \lesssim 40\xi$ ) is a poor analog to a classical laminar viscous sub-layer because it contains irregular vortex lines which terminate at the boundary.

In conclusion, our findings illustrate a deep analogy between classical and quantum fluids in the presence of boundaries, besides the analogies already noticed[1] in homogeneous isotropic turbulence. Our results also suggest that the walls which confine the flow of superfluid helium and the surfaces of moving objects used to generate turbulence (wires, grids, propellers, spheres) may be covered by a thin layer of tangled vortex lines. The experimental implications of such ‘superfluid boundary layer’ on macroscopic observables need to be investigated, particularly in  $^3\text{He-B}$ , where, due to relative large healing

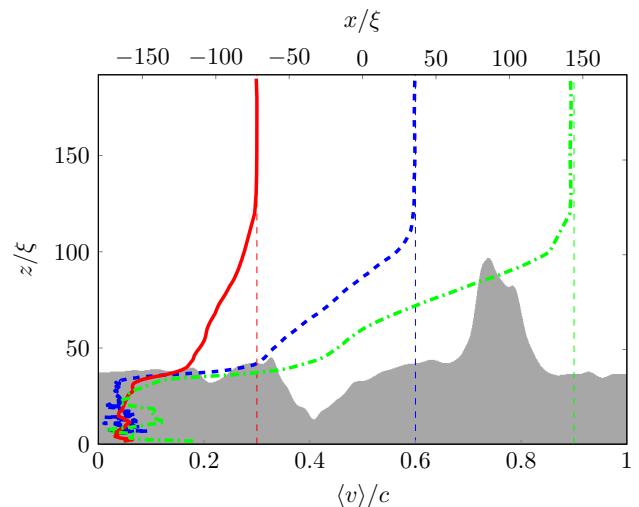


FIG. 5. Average superfluid velocity,  $\langle v \rangle$  (bottom scale), as a function of height,  $z$  (left scale), for  $v = 0.3c$  (solid red line),  $v = 0.6c$  (solid blue line), and  $v = 0.9c$  (dot-dashed green line) in the saturated regime. The grey surface silhouette is as in Fig. 3.

length, it is possible to control surface roughness.

We thank R. P. Haley and C. Lawson (Lancaster University) for providing the AFM image of their ‘floppy wire’. C.F.B. acknowledges funding from EPSRC (grant EP/I019413/1). This work used the facilities of N8 HPC, provided and funded by the N8 consortium and EPSRC (grant EP/K000225/1).

Data supporting this work is openly available under an Open Data Commons Open Database License [46].

## SUPPLEMENTARY MATERIAL

### Gross-Pitaevskii model of the superfluid

The superfluid is modelled as a weakly-interacting Bose gas. It is parameterised by a complex wavefunction  $\Psi(\mathbf{r}, t) = \sqrt{n(\mathbf{r}, t)} \exp[iS(\mathbf{r}, t)]$ , where  $n$  and  $S$  represent the distribution of the particle number density and phase, respectively. The wavefunction obeys the time-dependent Gross-Pitaevskii equation [47, 48],

$$i\hbar \frac{\partial \Psi}{\partial t} = \left( -\frac{\hbar^2}{2m} \nabla^2 + V(\mathbf{r}, t) + g|\Psi|^2 \right) \Psi. \quad (1)$$

where  $m$  denotes the particle mass, the coefficient  $g$  accounts for local particle interactions, and  $V(\mathbf{r}, t)$  describes a potential landscape acting on the fluid. The GPE is equivalent to a hydrodynamic model with fluid density  $n(\mathbf{r}, t) = |\Psi(\mathbf{r}, t)|^2$  and velocity  $\mathbf{v}(\mathbf{r}, t) = (\hbar/m)\nabla S$ , and embodies a classical continuity equation and a modified Euler equation (the modification being the presence of a quantum pressure term, arising from zero-point motion of the particles and responsible for vortex nucleation and reconnections).

Within the GPE model and assuming a homogeneous particle density  $n_0$ , the vortex core size is characterised by the healing length  $\xi = \hbar/\sqrt{mn_0g}$ . The natural speed, energy and time scales are provided by the speed of sound  $c = \sqrt{n_0g/m}$ , the chemical potential  $\mu = n_0g$  and the unit  $\tau = \xi/c$ , respectively.

### Set-up of the simulations

Our results are based on simulations of the GPE over the entire AFM surface, resolved down to a sub-core scale of  $\Delta = 0.4\xi$ . In  $^4\text{He}$  the vortex core size is  $a_0 \approx 10^{-10}$  m [49], such that the  $(1\mu\text{m})^2$  AFM image has true core dimensions  $(10^4 \times 10^4 \times 100)a_0^3$ . It is not computationally feasible to model the corresponding range of scales directly within the GPE; as such we map the AFM image onto the largest practical healing length volume of  $(400 \times 400 \times 100)\xi^3$ . This is simulated in a box of size  $(400 \times 400 \times 200)\xi^3$  (the numerical domain being twice as high as the highest mountain in the third dimension),

on a  $1000 \times 1000 \times 500$  spatial grid, which is periodic in  $x$  and  $y$ . Time evolution is performed with 4th order Runge-Kutta scheme with time step  $\Delta t = 0.01\tau$ , and performed across 256 (2.6 GHz) cores of a computer cluster. The rough surface is incorporated into the GPE by setting a potential barrier  $V = 5\mu$  below the surface, heavily prohibiting density there; above the surface the density recovers to the bulk value  $n_0$  (where  $V = 0$ ) over a lengthscale of the order of  $\xi$ .

We first obtain the stationary solution of the GPE in the presence of the rough boundary, with bulk density  $n_0$ , by solving the GPE in imaginary time [50]. The GPE is then transformed into a frame moving at speed  $u$  in the  $x$ -direction (corresponding to the imposed flow) by the addition of a Galilean boost term  $i\hbar u \partial \Psi / \partial x$  to the right-hand side of the GPE. The flow speed is ramped up smoothly from zero to the required final value.

### Emergent kinematic viscosity

We estimate the effective kinematic viscosity in the following way. Consider the volume  $V = D^2h$  where  $D = 200\xi$  is the extension in the  $x$  and  $y$  direction and  $h \approx 60\xi$  is approximately the height of the turbulent layer in the  $z$  direction. The energy that the uniform flow of speed  $v$  (along the  $x$  direction) brings into this volume in time  $\Delta t$  is  $E_{\text{in}} = \rho D h v^3 \Delta t / 2$ . In the turbulent layer, the velocity is not uniform, but is approximately  $vz/h$ . The energy which this shear flow takes out of the said volume is  $E_{\text{out}} = \rho D v^3 \Delta t / 8$ . In time  $\Delta t$ , the energy difference  $E_{\text{in}} - E_{\text{out}}$  is deposited into the turbulence. Since we are dealing with a statistical steady state, this energy is also dissipated into sound waves when vortices accelerate around each other [39] or reconnect [40] (including reconnections with images across the rough surface). For the sake of simplicity, we group the small vortex rings which are emitted by the turbulent layer with the sound waves.

In time  $\Delta t$ , the energy (per unit mass) dissipated by the turbulence is thus  $\Delta E' = (3/8h)v^3 \Delta t$ . Following Walmsley and Golov’s [41] analysis of their experiments in low-temperature  $\text{He}^4$ , we use the classical result that relates the rate of energy dissipation (per unit mass),  $dE'/dt$ , to the kinematic viscosity  $\nu$  and the vorticity  $\omega$  of the fluid,

$$\frac{dE'}{dt} = -\nu \omega^2. \quad (2)$$

We also make the identification [41]  $\omega \approx \kappa \mathcal{L}$  where  $\mathcal{L}$  is the vortex line density, defined as the vortex length  $L$  per unit volume  $V$  (for the sake of simplicity, we neglect the volume of the ‘mountains’ and identify  $V \approx D^2h$ ).

The ‘emergent kinematic viscosity’  $\nu$  of the superfluid’s turbulent layer can therefore be estimated from the balance between the energy (per unit mass per unit time),

$3v^3/(8h)$  which is fed into the turbulence by the incoming flow, and the energy (per unit mass per unit time)  $\nu\kappa^2\mathcal{L}^2$  which is dissipated into waves. It is convenient to express  $\nu$  in terms of the quantum of circulation  $\kappa$ . We obtain,

$$\frac{\nu}{\kappa} = \frac{3v^3}{8\kappa^3 D\mathcal{L}^2}. \quad (3)$$

In our dimensionless units based on  $\xi$  and  $c$ , the quantum of circulation is  $\kappa = 2\pi$ . At the three applied flow speeds we find that the saturated turbulent layer has length (see Fig. 3)  $L \approx 2000\xi, 7000\xi$  and  $15000\xi$  corresponding to  $\nu/\kappa = 2.4, 1.5$  and  $1.1$  respectively.

These values are larger than  $\nu/\kappa \approx 0.1$  reported [41] in experimental studies of the ‘Vinen’ (or ‘ultraquantum’) turbulent regime in He<sup>4</sup>. We argue that the explanation of this difference is that in the helium experiments the vortex lines are relatively farther away from each other. Since dissipation arises from sound emission from rapidly accelerating vortices and from vortex reconnections, we expect more dissipation in our problem.

To quantify the relative separation between the vortex lines, we compare the average intervortex distance  $\delta \approx \mathcal{L}^{-1/2}$  to the vortex core radius  $a_0$ , which is  $a_0 \approx 10^{-10}$  m in helium and  $a_0 \approx 5\xi$  in our problem. Clearly, at the smallest distance between two vortex lines,  $\delta \approx a_0$ , the two vortices either rotate around each other with speed approaching the speed of sound, or undergo a vortex reconnection, turning kinetic into acoustic energy at the highest rate.

Figure 3 of Ref. [41] shows vortex line density  $\mathcal{L} \approx 2 \times 10^7 \text{ m}^{-2}$ , which is typical of other He<sup>4</sup> experiments, yielding  $\delta/a_0 \approx 2 \times 10^6$ . In our problem, corresponding to the three imposed speeds, we find  $\delta/a_0 \approx 13.8, 7.4$  and  $5.1$ : the vortex lines are more closely packed, therefore it is not unexpected that in our problem the dissipation is larger.

---

\* george.stagg@newcastle.ac.uk

- [1] C. F. Barenghi, L. Skrbek, and K. R. Sreenivasan, *Proc. Nat. Acad. Sci. USA*, **111** (Suppl. 1), 4647 (2014).
- [2] D. I. Bradley, S. N. Fisher, A. M. Guénault, R. P. Haley, G. R. Pickett, G. Potts, and V. Tsepelin, *Nature Phys.* **7**, 473 (2011).
- [3] D. E. Zmeev, P. M. Walmsley, A. I. Golov, P. V. E. McClintock, S. N. Fisher and W. F. Vinen, *Phys. Rev. Lett.*, **115**, 155303 (2015).
- [4] L. Boué, V. L’vov, A. Pomyalov and I. Procaccia, *Phys. Rev. Lett.* **110**, 014502 (2013).
- [5] S. I. Davis, P. C. Hendry and P. V. E. McClintock, *Physica B (Cond. Matt.)* **280**, 43 (2000).
- [6] A. M. Guénault, V. Keith, C. J. Kennedy, S. G. Mussettt and G. R. Pickett, *J. Low Temp. Phys.* **62**, 511 (1986).
- [7] D. I. Bradley, D. O. Clubb, S. N. Fisher, A. M. Guénault, R. P. Haley, C. J. Matthews, G. R. Pickett, V. Tsepelin and K. Zaki, *Phys. Rev. Lett.* **95**, 035302 (2005).
- [8] D. I. Bradley, M. Človečko, M. J. Fear, S. N. Fisher, A. M. Guénault, R. P. Haley, C. R. Lawson, G. R. Pickett, R. Schanen, V. Tsepelin and P. Williams, *J. Low Temp. Phys.* **165**, 114 (2011).
- [9] S. N. Fisher, A. J. Hale, A. M. Guénault and G. R. Pickett, *Phys. Rev. Lett.* **86**, 244 (2001).
- [10] R. Blaauwgeers, M. Blazkova, M. Človečko, V. B. Eltsov R. de Graaf, J. Hosio, M. Krusius, D. Schmoranzler, W. Schoepe, L. Skrbek, P. Skyba, R. E. Solntsev and D. E. Zmeev, *J. Low Temp. Phys.* **146**, 537 (2007).
- [11] D. I. Bradley, M. Človečko, S. N. Fisher, D. Garg, E. Guise, R. P. Haley, O. Kolosov, G. R. Pickett, V. Tsepelin, D. Schmoranzler and L. Skrbek, *Phys. Rev. B* **85**, 014501 (2012).
- [12] J. Maurer and P. Tabeling, *Europhys. Lett.* **43**, 29 (1998)
- [13] J. Salort, C. Baudet, B. Castaing, B. Chabaud, F. Davidaud, T. Didelot, P. Diribarne, B. Dubrulle, Y. Cagne and F. Gauthier, *Phys. Fluids* **22**, 125102 (2010);
- [14] J. Jäger, B. Schudurer and W. Schoepe, *Phys. Rev. Lett.* **74**, 566 (1995).
- [15] W. F. Vinen and L. Skrbek, *Progress in Low Temperature Physics*, ed. by W.P. Halperin and M. Tsubota, Elsevier (Amsterdam), Vol XVI, Chap 4, pp 195-246 (2008).
- [16] D. E. Zmeev, F. Pakpour, P. M. Walmsley, A. I. Golov, W. Guo, D. N. McKinsey, G. G. Ihas, P. V. E. McClintock, S. N. Fisher and W. F. Vinen, *Phys. Rev. Lett.* **110**, 175303 (2013).
- [17] D. Duda, P. Švančara, M. La Mantia, M. Rotter and L. Skrbek, *Phys. Rev. B* **92**, 064519 (2015).
- [18] G. P. Bewley, D. P. Lathrop and K. R. Sreenivasan, *Nature* **441**, 588 (2006).
- [19] T. Xu and S. W. Van Sciver, *Phys. Fluids* **19**, 071703 (2007).
- [20] W. Guo, M. La Mantia, D. P. Lathrop and S. W. Van Sciver, *Proc. Nat. Aca. Sci. USA* **111**, Suppl. 1, 4653 (2014).
- [21] T. Frisch, Y. Pomeau, and S. Rica, *Phys. Rev. Lett.* **69**, 1644 (1992).
- [22] K. W. Schwarz, *Phys. Rev. Lett.* **64**, 1130 (1990).
- [23] K. W. Schwarz, *Phys. Rev. Lett.* **47**, 251 (1981).
- [24] M. Tsubota, *Phys. Rev. B* **50**, 579 (1994).
- [25] T. Winiński, PhD thesis, University of Durham (2001).
- [26] G. W. Stagg, N. G. Parker and C. F. Barenghi, *J. Phys. B* **47**, 095304 (2014).
- [27] N. Hashimoto, R. Goto, H. Yano, K. Obara, O. Ishikawa and T. Hata, *Phys. Rev. B* **76**, 020504(R) (2007).
- [28] C. R. Lawson, PhD thesis, Lancaster University (2013).
- [29] See Supplemental Material section at the end of this manuscript.
- [30] K. W. Schwarz, *Phys. Rev. B* **38**, 2398 (1988).
- [31] R. Hänninen, M. Tsubota and W. F. Vinen, *Phys. Rev. B* **75**, 064502 (2007).
- [32] D. Kivotides, C. F. Barenghi and Y. A. Sergeev, *Phys. Rev. B* **77**, 014527 (2008).
- [33] R. Hänninen and A. W. Baggaley, *Proc. Nat. Acad. Sci. USA* **111** (Suppl. 1), 4667 (2014).
- [34] R. Goto, S. Fujiyama, H. Yano, Y. Nago, N. Hashimoto, K. Obara, O. Ishikawa, M. Tsubota and T. Hata, *Phys. Rev. Lett.* **100**, 045301 (2008).
- [35] M. Kurasa, K. Bajaj and T. Lipniacki, *Phys. Rev. B* **83**, 014515 (2011).
- [36] R. M. Kerr, *Phys. Rev. Lett.* **106**, 224501 (2011).
- [37] B. V. Svistunov, *Phys. Rev. B* **52**, 3647 (1995).

- [38]  $\langle v \rangle$  is the  $x$ -component of the velocity averaged over the  $xy$  plane and 5 time steps in the saturated regime.
- [39] C. F. Barenghi, N. G. Parker, N. P. Proukakis and C. S. Adams, *J. Low Temp. Phys.* **138**, 629 (2005).
- [40] M. Leadbeater, T. Winiecki, D.C. Samuels, C.F. Barenghi and C.S. Adams, *Phys. Rev. Lett.* **86**, 1410 (2001).
- [41] P. M. Walmsley and A. I. Golov, *Phys. Rev. Lett.* **100**, 245301 (2008).
- [42] M. T. Reeves, T. P. Billam, B. P. Anderson and A. S. Bradley, *Phys. Rev. Lett.* **114**, 155302 (2015).
- [43] W. Schoepe, *JETP Lett.* **102**, 105 (2015).
- [44] K. Sasaki, N. Suzuki, and H. Saito, *Phys. Rev. Lett.* **104**, 150404 (2010).
- [45] W. J. Kwon, J. H. Kim, S. W. Seo and Y. Shin, *Phys. Rev. Lett.* **117**, 245301 (2016).
- [46] DOI to be provided once accepted.
- [47] “Bose-Einstein Condensation in Dilute Gases”, C. J. Pethick and H. Smith (Cambridge University Press, Cambridge, 2002)
- [48] P. H. Roberts and N. G. Berloff, in *Quantized vortex dynamics and superfluid turbulence*, eds C. F. Barenghi, R. J. Donnelly and W. F. Vinen, Springer (Berlin, Heidelberg) (2001), page 235–257.
- [49] Rayfield, G. W., and Reif, F. D. *Phys. Rev. A* **136**, A1194 (1964).
- [50] “A Primer in Quantum Fluids”, C. F. Barenghi and N. G. Parker (Springer, Berlin, 2016)